Journal of the Mechanics and Physics of Solids 60 (2012) 1363–1381

Contents lists available at SciVerse ScienceDirect

Journal of the Mechanics and Physics of Solids

journal homepage: www.elsevier.com/locate/jmps

A criterion for the onset of void coalescence under combined tension and shear

C. Tekoğlu [a,*], J.-B. Leblond [b], T. Pardoen [c]

[a] Department of Mechanical Engineering, TOBB University of Economics and Technology, Söğütözü, Ankara 06560, Turkey
[b] Institut Jean-Le-Rond-d'Alembert, Université Paris VI, Tour 65-55, 4, Place Jussieu, 75252 Paris Cedex 05, France
[c] Institute of Mechanics, Materials and Civil Engineering, Université catholique de Louvain, Place Sainte Barbe 2, B-1348 Louvain-la-Neuve, Belgium

ARTICLE INFO

Article history:
Received 24 June 2011
Received in revised form
23 January 2012
Accepted 19 February 2012
Available online 24 February 2012

Keywords:
Ductility
Fracture mechanisms
Voids and inclusions
Finite elements
Limit-load analysis

ABSTRACT

Depending on the relative positions of voids and on the loading conditions, shear loading components can play an important role in the void coalescence process leading to ductile fracture. Yet, most void coalescence criteria including the original criterion of Thomason, and its various extensions/improvements, take only normal loads into account and neglect the contribution from shear loads to coalescence. Shear can affect both the stress/strain at the onset of coalescence and the direction of deformation localization. In this paper, first, the predictive capabilities of different coalescence criteria without shear effect are critically assessed and the expressions involved in the original Thomason criterion are fine-tuned by comparing with 3D finite element calculations performed on a unit cell containing a spheroidal void. Then, the improved Thomason criterion is theoretically extended—by using limit load analysis—to incorporate the effect of shear. The predictions of this new coalescence criterion are in good agreement with the results produced by 3D finite element calculations, for both loadings involving or not a shear component.

1. Introduction

Macroscopic cracks leading to ductile failure initiate and propagate through coalescence of neighboring microscopic voids. During plastic deformation, voids grow and change shape as well as their relative position. Initially, i.e. in the course of stable void growth, plastic deformation is more or less uniformly distributed in the material. At some point, deformation localizes in the ligament connecting adjacent voids while the regions off the localization plane undergo elastic unloading. This sudden transition from uniform to localized plasticity is referred to as the onset of void coalescence. Three distinct modes of void coalescence have been repetitively observed: (i) internal necking, (ii) shear coalescence, and (iii) necklace coalescence.

The mode of coalescence depends on the relative positions of the voids as well as on the loading conditions. In *internal necking*, also referred to as coalescence in layers (e.g. Gologanu et al., 2001b), the localization plane is (almost) perpendicular to the main loading direction. With further deformation after the onset of void coalescence, the intervoid ligament shrinks in a way similar to a necking process in a macroscopic specimen under uniaxial tension. Internal necking is the most commonly observed mode of coalescence, and was the earliest to be discovered, see e.g. Argon et al. (1975) and references therein. The schematics in Fig. 1(a) and (b), respectively, show an idealized material containing regularly

* Corresponding author. Tel.: +90 312 292 42 29; fax: +90 312 292 40 91.
E-mail addresses: cihantekoglu@etu.edu.tr, C.Tekoglu@gmail.com (C. Tekoğlu).

0022-5096/$ - see front matter
doi:10.1016/j.jmps.2012.02.006

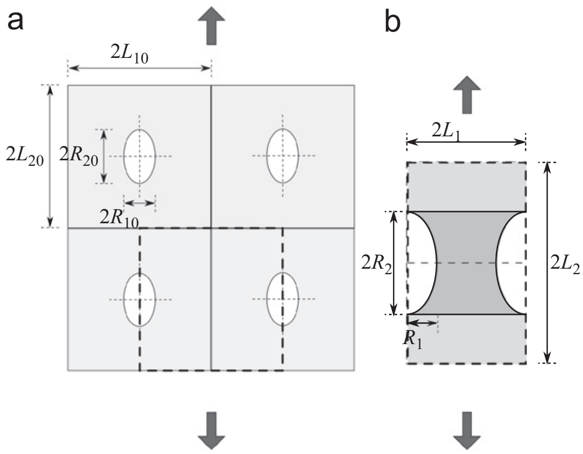

Fig. 1. (a) An idealized material containing regularly distributed spheroidal voids – each located at the center of a cubic unit cell – in the undeformed configuration. (b) Plastic localization in the intervoid ligament at the onset of internal necking for the material shown in (a).

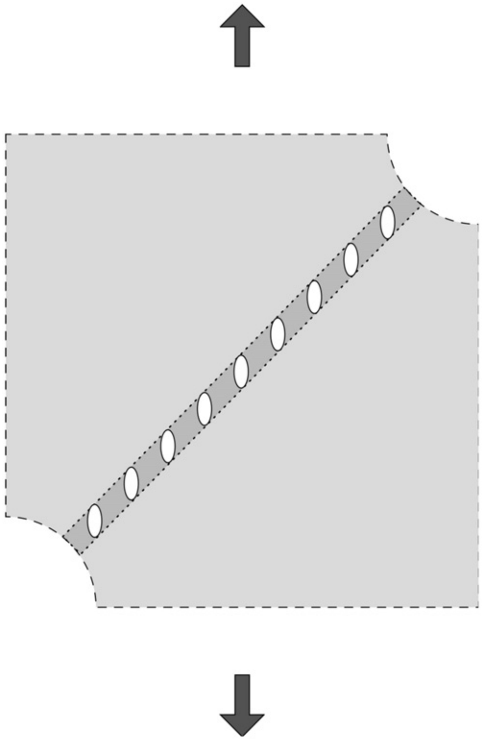

Fig. 2. Plastic localization in a microshear band during "void sheeting".

distributed spheroidal voids – each located at the center of a cubic unit cell – in the undeformed configuration and the plastic localization in the intervoid ligament at the onset of internal necking.

The second most observed mode of coalescence is *shear coalescence*, which often occurs through the so-called "void sheeting" mechanism (e.g. Cox and Low, 1974; Bandstra and Koss, 2001). As illustrated in Fig. 2, in void sheeting plasticity localizes in microscopic shear bands containing small secondary voids; large primary voids are linked through coalescence of these secondary voids. In their series of papers (Tvergaard, 2008, 2009; Tvergaard and Nielsen, 2010; Nielsen and Tvergaard, 2011), Nielsen and Tvergaard recently brought out this mechanism for ductile materials subject to intense shearing. However, shear coalescence can also intervene without any secondary voids. Richelsen and Tvergaard (1994) investigated the competition between shear coalescence and internal necking as a function of stress triaxiality and material properties.

Necklace coalescence, or coalescence in columns, as illustrated in Fig. 3, is distinguished from internal necking by the fact that, as opposed to internal necking, the localization band is (almost) parallel to the main loading axis (Benzerga, 2000; Gologanu et al., 2001a). This mode of coalescence occurs between row of voids elongated in the main loading direction and

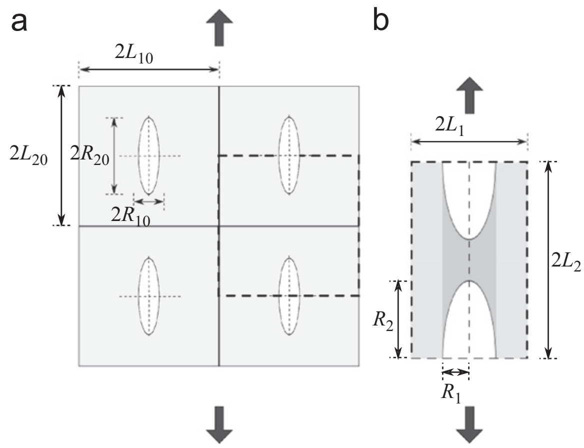

Fig. 3. (a) An idealized material containing regularly distributed spheroidal voids – each located at the center of a cubic unit cell – in the undeformed configuration. (b) Plastic localization in the intervoid ligament at the onset of necklace coalescence for the material shown in (a). Note that, necklace coalescence is distinguished from internal necking by the fact that, as opposed to internal necking, the localized deformation band is parallel to the main loading axis.

has a smaller effect on macroscopic ductility; yet, it is believed to be a key mechanism in ductile delamination (Benzerga et al., 2004).

The void growth rate during the "void coalescence phase" is much larger than the growth rate during the stable "void growth phase". For many materials, especially under moderate or low stress triaxiality, the macroscopic strain increment during the void coalescence phase up to fracture is rather small. Therefore, in many ductile damage models, the fracture strain is safely assumed to correspond to the value at the onset of void coalescence (e.g. Simar et al., 2010; Tekoğlu and Pardoen, 2010). At high stress triaxiality, however, the increase in the macroscopic strain during coalescence can reach values comparable to or even higher than the strain accumulated in the pre-coalescence regime; this requires employing two different yield functions for the pre-coalescence and coalescence phases (e.g. Benzerga, 2002; Pardoen, 2006; Pardoen and Hutchinson, 2003; Scheyvaerts et al., 2010). The onset of coalescence has to be accurately determined either to be used as the fracture criterion, or to distinguish pre-coalescence and coalescence phases.

Various criteria have been postulated to determine the onset of void coalescence. The most widely used phenomenological criterion relates the initiation of void coalescence to a critical porosity, whose value is assumed to depend on the material, but not on the loading condition (e.g. McClintock, 1968, 1971; Tvergaard, 1990; Marini et al., 1985). Although it is well known that the porosity at the onset of coalescence for a material depends on the stress triaxiality T (e.g. Pardoen and Hutchinson, 2000), this criterion is acceptable from a practical standpoint, especially for low-porosity alloys with a well-defined microstructure, at least in a limited range of T. Another phenomenological criterion states that fracture initiates rapidly after the maximum effective stress has been reached (e.g. Becker, 1987; Koplik and Needleman, 1988); this criterion is limited to radial loading conditions and shown to be acceptable only at low stress triaxiality. An early micromechanics based criterion postulated by Brown and Embury (1973) states that, for a perfectly plastic material, internal necking sets in when it becomes possible for two neighboring voids to be connected by microshear bands orientated at 45° from the principal axis of the intervoid ligament. The criterion of Brown and Embury is shown to provide qualitatively acceptable results (e.g. Pardoen et al., 1998).

A more rigorous micromechanical treatment of the onset of internal necking is given by the pioneering works of Thomason (see Thomason, 1990 and references therein). According to Thomason's criterion, internal necking initiates when a plastic limit load is attained. The original criterion of Thomason, for elastic-perfectly plastic solids, is further improved and extended for strain hardening materials by several investigators (e.g. Benzerga, 2000, 2002; Fabrègue and Pardoen, 2008, 2009; Lecarme et al., 2011; Pardoen and Hutchinson, 2000; Pardoen et al., 2010; Yerra et al., 2010). A detailed review of void coalescence, concerning both experimental and theoretical studies can be found in Benzerga and Leblond (2010), Pardoen and Bréchet (2004), or Pineau and Pardoen (2007).

Neither the original criterion of Thomason, nor its extensions/improvements take into account the contribution of shear components on the onset of void coalescence. However, depending on the relative positions of voids and loading conditions, significant shear loads might arise in the intervoid ligament, and play an important role in internal necking, affecting both the stress/strain value required for the onset of coalescence and the orientation of the localization process. Limit load analysis for void coalescence under combined tension and shear has been previously performed by Leblond and Mottet (2008). However, unlike Thomason, Leblond and Mottet (2008) did not define a detailed velocity field over the representative volume element (RVE). Instead, they employed an RVE that corresponds to a "sandwich" made of three superposed planar layers, sound/porous/sound (see also Perrin, 1992), and assumed that, during coalescence the sound layers become rigid while the central porous layer obeys a Gurson type yield criterion. It is worth reminding the remark of

Leblond and Mottet (2008): "Another, probably more theoretically satisfactory possibility, would be to describe it (*the behavior of the porous layer*) through some suitable extension of Thomason's treatment of coalescence (based on detailed analysis of the microscopic velocity field around the void) to non-axisymmetric loadings. It is not clear, however, that such an extension could be achieved, considering the complexity of Thomason's analysis in the simpler case he considered". The main goal of this paper is to achieve this extension.

The paper is organized as follows. Section 2 gives a detailed description of the finite element (FE) calculations performed on 3D RVE's containing a spheroidal void at the center. In Section 3, the micromechanics based criterion for the onset of void coalescence of Brown and Embury, that of Thomason, as well as the extension of the Thomason's criterion by Benzerga, are first briefly summarized and then their predictions are compared with the results of the 3D FE calculations. The coefficients involved in the criteria of Thomason and of Benzerga are then fine-tuned through comparison with the FE calculations. In Section 4, the original Thomason criterion is extended to non-axisymmetric loadings; the extended criterion is also validated by comparing with the 3D FE calculations, involving a shear component. Section 5 briefly discusses the results, and finally, Section 6 underlines the main conclusions of this work.

2. 3D FE calculations with a voided unit cell

Since the seminal works of Needleman (1972) and Koplik and Needleman (1988), finite element calculations performed on model materials containing periodically distributed voids constitute a widely used method to investigate microscopic mechanisms involved in the growth and coalescence of voids. The benefit of such FE calculations is clear considering the difficulties in making in situ experiments of void growth rate in real materials. Most of these computational studies assume a hexagonal lattice type periodicity for the initial void distribution, where the resulting RVE is a hexagonal cylindrical unit cell with a void located at the center. The advantage of this is that a hexagonal cylinder can be closely approximated by a circular one, which allows 2D axisymmetric calculations and thus reduces computational costs considerably (see e.g. Kuna and Sun (1996) and references therein). However, non-axisymmetric loadings – involving shear components – that will be investigated in this study require use of a 3D model. Following Thomason (1985), we assume here that the void centers correspond to the lattice points of a simple (primitive) cubic system in the undeformed configuration. The simplest RVE for this void distribution is a cubic unit cell, as the unit cells shown in Figs. 11 and 12.

The initial edge lengths of the unit cell are $2L_{10}=2L_{20}=2L_{30}$, which are aligned along the coordinate axes x_i $(i=1,2,3)$. The void, which is located at the center of the unit cell, is assumed to be spheroidal, and

$$W_0=\frac{R_{20}}{R_{10}}=\frac{R_{20}}{R_{30}},\quad \chi_0=\frac{R_{10}}{L_{10}}=\frac{R_{30}}{L_{30}},\quad f_0=\frac{\pi}{6}\frac{R_{10}R_{20}R_{30}}{L_{10}L_{20}L_{30}},\tag{1}$$

where W_0 and χ_0 are defined to be the initial void aspect ratio and relative void spacing, respectively, and f_0 is the initial porosity (f_0 can simply be deduced from geometric considerations).

The matrix material is elastic-perfectly plastic with a Young's modulus over yield stress ratio $E/\sigma_0=444.5$ and a Poisson ratio $\nu=0.49$. Theoretical limit load analysis of a structure corresponds to a problem of a rigid, perfectly plastic material, where the velocity field in the material is incompressible. Therefore, without loss of generality, we employed an admittedly high value for the Poisson ratio in order to ensure near elastic incompressibility.[1] If a realistic Poisson ratio – around $\nu=0.3$ for many metals – is used, the velocity field obtained after the first elastoplastic iteration is not at all incompressible. Many iterations are then necessary to gradually modify this field to make it satisfy the incompressibility condition. A high value of Poisson ratio, $\nu=0.49$, ensures that the first elastoplastic iteration produces an almost incompressible velocity field, a condition that has to be satisfied in limit analysis. In this sense, taking $\nu=0.49$ facilitates numerical convergence.

However, it is well known from the computational mechanics literature that if ν is not taken to be "sufficiently far" from 0.5, the stiffness matrix becomes ill conditioned, and this generates numerical problems. The experience of the authors shows that taking $\nu=0.49$ is much more beneficial than detrimental; i.e. $\nu=0.49$ is sufficiently far from 0.5, and it does not cause numerical problems.

The FE calculations are performed using the commercial software ABAQUS. A Python script is written to automate the mesh generation, and 8-node linear brick elements (C3D8) are used for the mesh. Ten different void aspect ratio values are analyzed ($W_0=0.2,0.5,0.625,0.75,0.875,1,1.5,2,2.5,3$), with 10 different relative void spacing values for each case ($\chi_0=0.05l$, with $l=5,\ldots,14$).

For some $W-\chi$ sets, the void does not fit into a cubic unit cell. In such cases, the unit cell is enlarged in the x_2 direction, i.e. $L_{10}/L_{30}=1$ while $L_{20}/L_{10}>1$. Note that during void coalescence the regions off the intervoid ligament (the regions above and below the void; see Fig. 8) are rigid and have no influence on the stress state in the ligament. However, if the void is very close to the top (and bottom) boundaries, coalescence occurs in the x_2-x_3 plane (necklace coalescence), instead of x_1-x_3 plane (internal necking). Therefore, the L_{20}/L_{10} ratio is chosen large enough to avoid necklace coalescence; otherwise, the height of the unit cell has no influence on the results. Table 1 gives the L_{20}/L_{10} ratios for the configurations where this value had to be taken larger than 1.

[1] A classical result of limit-analysis is that when the limit-load is reached, the local elastic strains cease to vary. Therefore, when the limit-load is reached, the elastic strain rates (which are zero) disappear from the equations of the problem. Consequently, the elastic moduli also disappear; plasticity implies incompressibility, and the limit-load is independent of the values of the elastic moduli.

Table 1
$W-\chi$ sets for which $L_{20}/L_{10}>1$.

W	χ	$\frac{L_{20}}{L_{10}}$
1.5	$0.65\le\chi\le0.7$	1.2
2.0	$0.45\le\chi\le0.7$	1.6
2.5	$0.35\le\chi\le0.7$	2
3.0	$0.25\le\chi\le0.7$	2.4

Although, in general, second-order elements can successfully capture stress/strain concentrations as those that naturally arise in a unit cell with a void, we decided to use C3D8 (8-node linear brick) elements in the FE calculations. The reason is that, here we are dealing with almost incompressible material behavior, with $\nu=0.49$; the fully integrated quadrilateral and brick elements without the hybrid formulation, such as C3D20 (20-node quadratic brick), cannot handle the incompressible behavior as they tend to become over-constrained with increasing incompressibility, see ABAQUS (2008a). Using hybrid elements, such as C3D20H (20-node quadratic brick, hybrid with linear pressure), on the other hand, is beneficial only if the material behavior is fully incompressible, or almost incompressible and hyperelastic (ABAQUS, 2008a): as hybrid elements have more internal variables than their non-hybrid counterparts, they are also computationally more expensive, and for almost incompressible elastic–plastic materials and for compressible materials, the advantage they offer is not sufficient. For all these reasons, C3D8 is the most suitable element for the FE calculations performed in this study. For each $W-\chi$ set, a separate mesh convergence study is performed to ensure that the results are effectively mesh invariant.

The macroscopic stress state of the unit cell, Σ, consists of a predominant axial stress ($\Sigma_{22}>\Sigma_{11}$, $\Sigma_{22}>\Sigma_{33}$), plus an additional shear component (Σ_{12}). In order to achieve this, displacement boundary conditions are applied by imposing the strains $E_{11}=E_{33}$ and $E_{12}=R_{sh}E_{22}$, where R_{sh} defines the relative amount of shear strain. Note that similar FE simulations involving shear stress components have also been performed, for instance, by Leblond and Mottet (2008) and Scheyvaerts et al. (2011); a detailed description of the boundary conditions can be found in Scheyvaerts et al. (2011).[2] Owing to the symmetries involved in the loading conditions and the RVE, only one-forth of the unit cell needs to be meshed; for $R_{sh}=0$, i.e. for no shear contribution ($\Sigma_{12}=0$), it is even enough to mesh only one-eighth of the unit cell.

The stress is measured with respect to the initial (undeformed) configuration. The overall stress components Σ_{ij} are calculated by looping over all elements: $\Sigma_{ij}=\sum_{e=1}^{N}\left(\sum_{k=1}^{n}\sigma_{ij}^{k}\,\upsilon^{k}\right)^{e}/\sum_{e=1}^{N}\left(\sum_{k=1}^{n}\,\upsilon^{k}\right)^{e}$, where N is the total number of elements, n is the number of integration points in an element (n=8 for C3D8), σ_{ij} and υ are, respectively, the local stress and volume values at the corresponding integration point. The macroscopic strain is defined as $E_{ii}=U_i/(2L_{i0})$ and $E_{12}=U_t/(2L_{20})$, where U_i and U_t are, respectively, the normal and shear displacements applied at the boundaries of the unit cell, and L_{i0} are initial edge lengths of the unit cell ($i=1,2,3$).

The purpose of limit load analysis, by definition, is to determine the overall yield criterion for a given, specific configuration, which, in this study, corresponds to a specific set of void aspect ratio W and relative void spacing χ. Therefore, in the FE calculations, the shape/size changes of the voids arising from the displacements need to be avoided. In order to bypass the void growth phase and reach the onset of void coalescence at the well-defined initial configuration with a perfect spheroidal void shape, the calculations are performed by switching off the non-linear geometry option in ABAQUS (NLGEOM=No; for technical details see ABAQUS, 2008b). As the equilibrium equations are solved on the initial geometry instead of the deformed one (NLGEOM=No), $W=W_0$ and $\chi=\chi_0$.

In limit analysis, the defined velocity field contains a positive multiplicative constant. The equivalent of this property in the FE calculations performed here is that the absolute values of the displacements applied at the boundaries of the unit cell (U_i and U_t) have no consequence, as long as they are large enough so that the order of magnitude of the elastic strains in the unit cell is much smaller than the order of magnitude of the plastic strains (see Appendix for a detailed explanation of the relationship between the equations of limit-load analysis and of the time-discretized finite element method). Applying smaller (respectively, larger) displacements at the boundaries leads to smaller (respectively, larger) local displacements by the same factor, but the stress field does not change. Therefore, the strains mentioned in the text and represented in the figures are, in essence, measured with arbitrary units. This point is further explored in Section 5.

3. Micromechanics based criteria for the onset of void coalescence under tension

In this section we will first briefly review three micromechanics based criteria for void coalescence through internal necking: (i) Brown and Embury (1973), (ii) Thomason (1990), and (iii) the extension of Thomason's criterion by Benzerga

[2] Although the FE calculations in Scheyvaerts et al. (2011) are performed under "overall plane strain conditions", the boundary conditions given in the appendix of Scheyvaerts et al. (2011) represent the most general 3D case, and are used in calculations described in this paper. Also, one may note that, for $R_{sh}=0$, imposing $E_{11}=E_{33}$ leads to $\Sigma_{11}=\Sigma_{33}$; for $R_{sh}\neq0$, however, the shear stress Σ_{12} is also different than zero and therefore the x_1 and x_3 axes are not equivalent: although $E_{11}=E_{33}$, $\Sigma_{11}\neq\Sigma_{33}$.

(2000, 2002). All three criteria assume that the RVE is subjected to a predominant axial stress state ($\Sigma_{22} > \Sigma_{11}$, $\Sigma_{22} > \Sigma_{33}$, no shear components), where the x_2 direction is perpendicular to the main axis of the intervoid ligament. Starting with the onset of internal necking, plasticity is confined in the intervoid ligament. The regions below and above the void remain quasi-rigid and unload elastically; therefore, the RVE goes through pure extension in the x_2 direction, while macroscopic strains are zero in the lateral (x_1 and x_3) directions.

Both the criterion of Brown and Embury and that of Thomason are originally built for elastic-perfectly plastic materials. Several studies investigated the validity of these criteria (and their extensions) in comparison with mainly 2D axisymmetric FE unit cell calculations for strain hardening materials, or with experiments (see Section 1). However, authors are unaware of such a comparison performed with 3D FE calculations for elastic-perfectly plastic materials, for which these criteria are supposed to produce the best agreement. This comparison will be performed in this section, and it will allow fine-tuning of the coefficients involved in the original Thomason's criterion, before extending it for combined tensile and shear loadings.

3.1. The criterion of Brown and Embury

Due mainly to its simplicity, the coalescence criterion of Brown and Embury is widely used in the literature, especially for qualitative analysis. This criterion states that coalescence starts when two voids are close enough to be connected by microshear bands aligned at 45° to the main axis of the intervoid ligament. For a spheroidal void in the deformed configuration, this condition is met when

$$\chi = \frac{1}{\sqrt{W^2+1}}. \tag{2}$$

3.2. The criterion of Thomason

In his 3D analyzes, Thomason employed a cubic RVE, as the unit cells shown in Figs. 11 and 12, but with a square cuboid void at the center to simplify the formulation of the velocity fields. The coalescence condition then has the form

$$\frac{\Sigma_{22}}{\sigma_0} = C_f \frac{A_l}{A_s}, \tag{3}$$

where A_l is the area of the plane containing the intervoid ligament ($x_2 = 0$ plane in Figs. 11 and 12), A_s is the area of the top surface of the unit cell ($x_2 = L_2$ plane in Figs. 11 and 12), C_f is the plastic constraint factor which accounts for the change in the load carrying capacity of the surface A_l due to the presence of the void, σ_0 is the yield stress of matrix material, and Σ_{22} is the normal stress acting on the surface A_s. Postulating kinematically admissible, incompressible velocity fields in the segment of the RVE containing the intervoid ligament (note again that the regions off the segment are rigid), Thomason calculated upper bound estimates for Σ_{22} for various different intervoid ligament geometries. The following empirical expression was suggested for the plastic constraint factor C_f

$$C_f = \alpha\left(\frac{R_2}{L_1-R_1}\right)^2 + \beta\left(\frac{R_1}{L_1}\right)^{-1/2}, \tag{4}$$

stating that taking the constants $\alpha = 0.1$ and $\beta = 1.2$ produces the best agreement with the calculated Σ_{22} values. Inserting the definition for the void aspect ratio and relative mean void spacing defined from Eq. (1), Thomason's criterion reduces to the following form for the cubic primitive unit cell

$$\frac{\Sigma_{22}}{\sigma_0} = (1-\eta\chi^2)\left[\alpha\left(\frac{1-\chi}{W\chi}\right)^2 + \beta\frac{1}{\sqrt{\chi}}\right], \tag{5}$$

where η depends on A_l/A_s; for a cubic unit cell $\eta = \pi/4$, for a circular cylindrical (axisymmetric) unit cell $\eta = 1$.

3.3. Extension of Thomason's criterion by Benzerga

Benzerga (2000, 2002) pointed out a drawback of Eq. (5): when W goes to zero, Σ_{22} goes to infinity, i.e. Eq. (5) predicts no coalescence for very flat voids, irrespective of the value of the relative void spacing χ. This contradicts experimental observations showing that, when loaded normal to their plane, flat cavities and penny-shaped cracks are the most harmful. In order to solve this problem, Benzerga (2000, 2002) suggested an empirical modification to Eq. (5) as

$$\frac{\Sigma_{22}}{\sigma_0} = (1-\eta\chi^2)\left[\alpha\left(\frac{\chi^{-1}-1}{W^2+0.1\chi^{-1}+0.02\chi^{-2}}\right)^2 + \beta\frac{1}{\sqrt{\chi}}\right], \tag{6}$$

with $\alpha = 0.1$ and $\beta = 1.3$. Note however that, in most practical problems, flat voids nucleated with a small aspect ratio W tend to open quite fast and the aspect ratio at the onset of coalescence is often not so small as to require the corrected model (see e.g. Lassance et al., 2006).

3.4. Comparison with the FE calculations

For the calculations in this section, $R_{sh}=E_{12}/E_{22}=0$ and $E_{22}>E_{11}=E_{33}$, i.e. $\Sigma_{22}>\Sigma_{11}=\Sigma_{33}$ with no shear stress contribution (see Section 2 for the technical details on the FE calculations). Fig. 4(a) shows the evolution of normalized axial stress acting on the unit cell, Σ_{22}/σ_0, as a function of the stress triaxiality T, for W=0.5 with $\chi=0.4$ and 0.6. The stress triaxiality is defined as $T=\Sigma_h/\Sigma_{eq}$, where Σ_h and Σ_{eq} are the hydrostatic and equivalent stresses, respectively. For each calculation – i.e. each data point in Fig. 4(a) – a different $|E_{11}/E_{22}|$ ratio is imposed corresponding to a different stress triaxiality T; T increases with decreasing $|E_{11}/E_{22}|$ ratio, see Fig. 4(b). Note again that absolute values of the displacements applied at the boundaries of the unit cell (U_i and U_t), i.e. absolute values of the strains E_{ij}, do not matter as long as they are large enough so that the elastic strains in the unit cell are much smaller compared to the plastic strains. This point is further explored in Section 5. For both $\chi=0.4$ and $\chi=0.6$, Σ_{22} initially increases with increasing T and converges to a value, Σ_{22}^c, when the triaxiality is large enough and $|E_{11}|=|E_{33}|\simeq 0$. Σ_{22}^c corresponds to the axial stress value required to initiate coalescence for this specific void configuration (i.e. $W-\chi$ values); this is the procedure to determine the onset void coalescence for the FE calculations performed in this paper. For the void configuration and distribution addressed here, coalescence always occurs in the x_1-x_3 plane, and Σ_{22} is the macroscopic stress normal to the ligament connecting the neighboring voids (see Section 5 for a detailed discussion about the shape and size of the localized plastic deformation band.)

Fig. 5(a) shows the evolution of χ values at the onset of void coalescence as a function of W predicted by the criterion of Brown and Embury. The criterion of Brown and Embury is purely geometric; without explicitly taking into account the state of stress, it states that for a certain void aspect ratio W, there is a minimum relative intervoid distance χ above which coalescence initiates, and for smaller χ values coalescence would not occur irrespective of the value of the axial stress Σ_{22}. For instance, according to the criterion of Brown and Embury, for W=0.5 only $\chi\geq 0.894$ leads to coalescence (see the triangular data point in Fig. 5(a)). Fig. 5(b) plots the minimum stress triaxiality required to initiate coalescence, T_{min}^c, as given by the FE calculations (square data points), for several χ values with W=0.5. T_{min}^c increases with decreasing χ value; as opposed to the prediction of the criterion of Brown and Embury, coalescence thus occurs for every χ value analyzed. A line is also fitted to the FE data ($\chi=-0.1493T_{min}^c+0.9532$) in order to extrapolate and predict T_{min}^c for χ values that fall outside the range evaluated in this paper. For W=0.5 and $\chi=0.894$, $T_{min}^c=0.396$ (see the triangular data point). This supports the findings of other works (e.g. Pardoen et al., 1998) that the criterion of Brown and Embury provides acceptable results only at low stress triaxiality, but not at moderate to high stress triaxiality. Note that a more quantitative assessment would require comparing the coalescence strains.

Fig. 5(c) and (d) compare the FE results with the original criterion of Thomason, and the extension of Thomason's criterion by Benzerga, respectively, in terms of the evolution of Σ_{22}^c/σ_0 as a function of χ, for different W values. The data points represent the results of the FE calculations, while the solid lines represent Eq. (5) (with $\alpha=0.1$ and $\beta=1.2$) in (c), and Eq. (6) (with $\alpha=0.1$ and $\beta=1.3$) in (d). The results of the FE calculations clearly show that coalescence occurs for all $W-\chi$ sets: for the same W (respectively, χ) value, a smaller χ (respectively, W) value requires a larger Σ_{22}^c/σ_0 to initiate coalescence, hence a higher stress triaxiality. As W gets larger, Σ_{22}^c/σ_0 for the same χ values gets closer to each other: for W=2.5 and W=3, the FE data points are almost coincident in the entire χ regime. Similarly, as χ gets larger, the FE data points for different W values approach each other. Fig. 5(c) shows that, for $W\leq 0.5$, the original criterion of Thomason leads to poor predictions; it severely overestimates (respectively, underestimates) the FE data for small (respectively, large) χ values. The modification of Benzerga is indeed capable of avoiding this overestimation in the small $W-\chi$ regime, see Fig. 5(d). Yet, except for W=0.2 and $\chi\leq 0.4$, Benzerga's criterion underestimates the FE data in the entire χ regime for $W\leq 2$, while its predictions diverge more and more from the FE data with increasing χ. For $W>2$, both criteria provide relatively good predictions; the original Thomason's criterion does a slightly better job compared to the extension by Benzerga, which has a tendency to overestimate the FE data, mainly for $\chi>0.35$. Note again that a full assessment of the accuracy would require comparing the strains at coalescence.

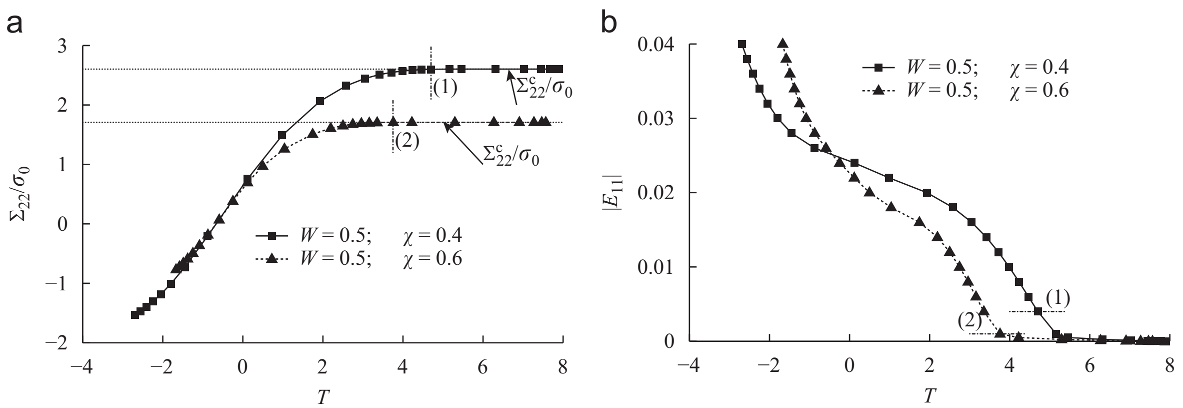

Fig. 4. Evolution of (a) Σ_{22}/σ_0 and (b) $|E_{11}|$ as a function of stress triaxiality T. Note that Σ_{22}^c corresponds to the axial stress value required to initiate coalescence for that specific void configuration (i.e. W,χ values), and the data points at (1) and (2), respectively, indicate the minimum stress triaxiality (and corresponding $|E_{11}|$ value) to initiate coalescence for $\chi=0.4$ and $\chi=0.6$.

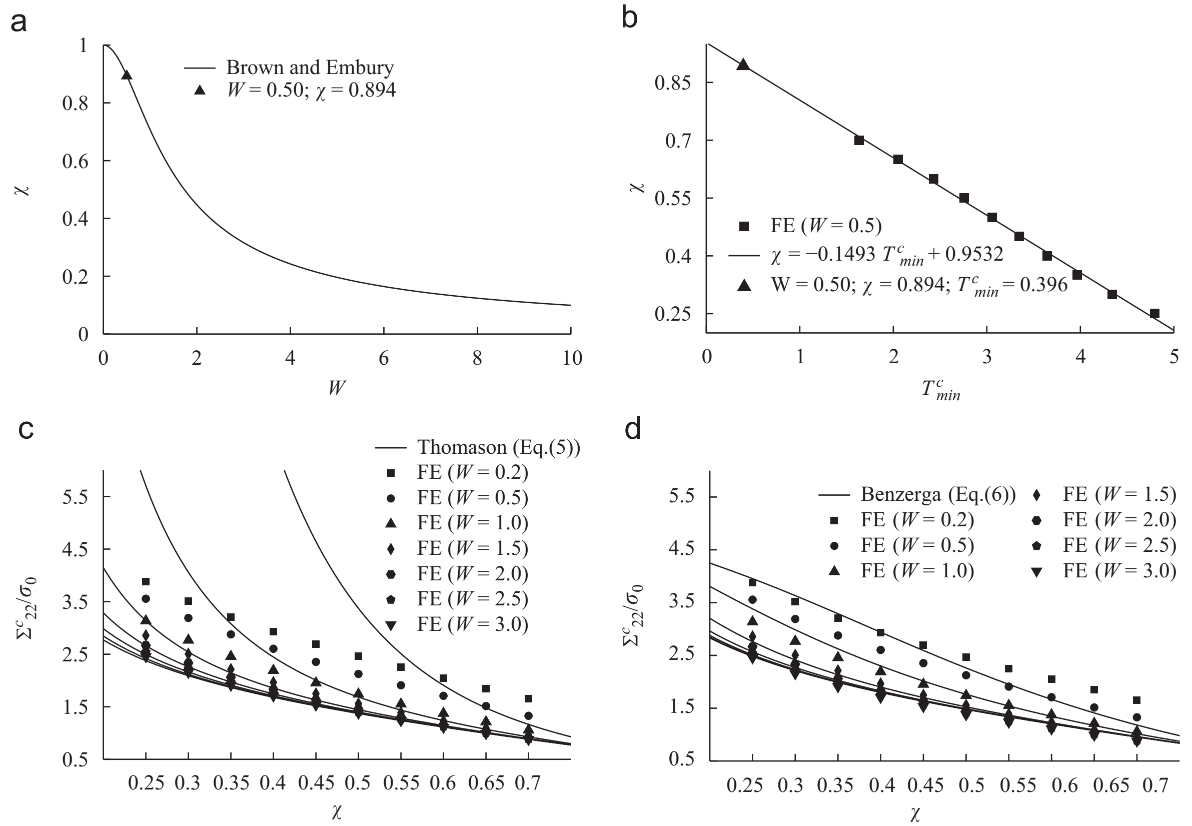

Fig. 5. (a) Predictions of the Brown and Embury criterion for the W and χ values at the onset of void coalescence. (b) For $W=0.5$, the minimum stress triaxiality required to initiate coalescence, T^c_{min}, for each χ value, as given by the FE calculations (square data points). For $W=0.5$ and $\chi=0.894$, $T^c_{min}=0.396$. Comparison of the finite element results for the evolution of Σ^c_{22}/σ_0 as a function of χ, for different W values with: (c) the original criterion of Thomason and (d) the extension of Thomason's criterion by Benzerga. The data points represent the results of the FE calculations, while the solid lines represent Eq. (5) (with $\alpha=0.1$ and $\beta=1.2$) in (c) and Eq. (6) (with $\alpha=0.1$ and $\beta=1.3$) in (d).

Before proceeding with extension of the coalescence criterion for general loading conditions, we first fine-tune the parameters α and β in Eqs. (5) and (6) as a function of W in order to best fit the FE data for coalescence under tension. As the criterion of Brown and Embury provides rather poor predictions – it does not contain any information on the stress state – we will no longer pursue this criterion.

Fig. 6(a) and (b) show, respectively, the best fits of the original criterion of Thomason, Eq. (5), and the extension of Thomason's criterion by Benzerga, Eq. (6), to the results of the FE calculations. The fits are obtained by fine-tuning the parameters α and β for the corresponding W value. Fig. 7(a) and (b) show the evolution of α and β as a function of W, for Thomason's and Benzerga's criterion, respectively. For Thomason's criterion, $\alpha^{Th}(W)$ (respectively, $\beta^{Th}(W)$) can be obtained by fitting a line (respectively, a fifth order polynomial) to the data points:

$$\alpha^{Th}(W)=0.0819W-0.0373,\ \ \beta^{Th}(W)=0.0036W^5-0.0030W^4-0.1694W^3+0.8499W^2-1.6743W+2.5022. \tag{7}$$

Similarly, for Benzerga's criterion, $\alpha^{Be}(W)$ (respectively, $\beta^{Be}(W)$) can be obtained by fitting a third order polynomial (respectively, a fifth order polynomial) to the data points:

$$\begin{aligned}&\alpha^{Be}(W)=0.0426W^3+0.1153W^2+0.0060W-0.0312,\\&\beta^{Be}(W)=-0.0616W^5+0.5814W^4-2.1409W^3+3.9303W^2-3.8402W+3.0035.\end{aligned} \tag{8}$$

In their new forms, both the criterion of Thomason

$$\frac{\Sigma_{22}}{\sigma_0}=(1-\eta\chi^2)\left[\alpha^{Th}(W)\left(\frac{1-\chi}{W\chi}\right)^2+\beta^{Th}(W)\frac{1}{\sqrt{\chi}}\right], \tag{9}$$

and the criterion of Benzerga

$$\frac{\Sigma_{22}}{\sigma_0}=(1-\eta\chi^2)\left[\alpha^{Be}(W)\left(\frac{\chi^{-1}-1}{W^2+0.1\chi^{-1}+0.02\chi^{-2}}\right)^2+\beta^{Be}(W)\frac{1}{\sqrt{\chi}}\right], \tag{10}$$

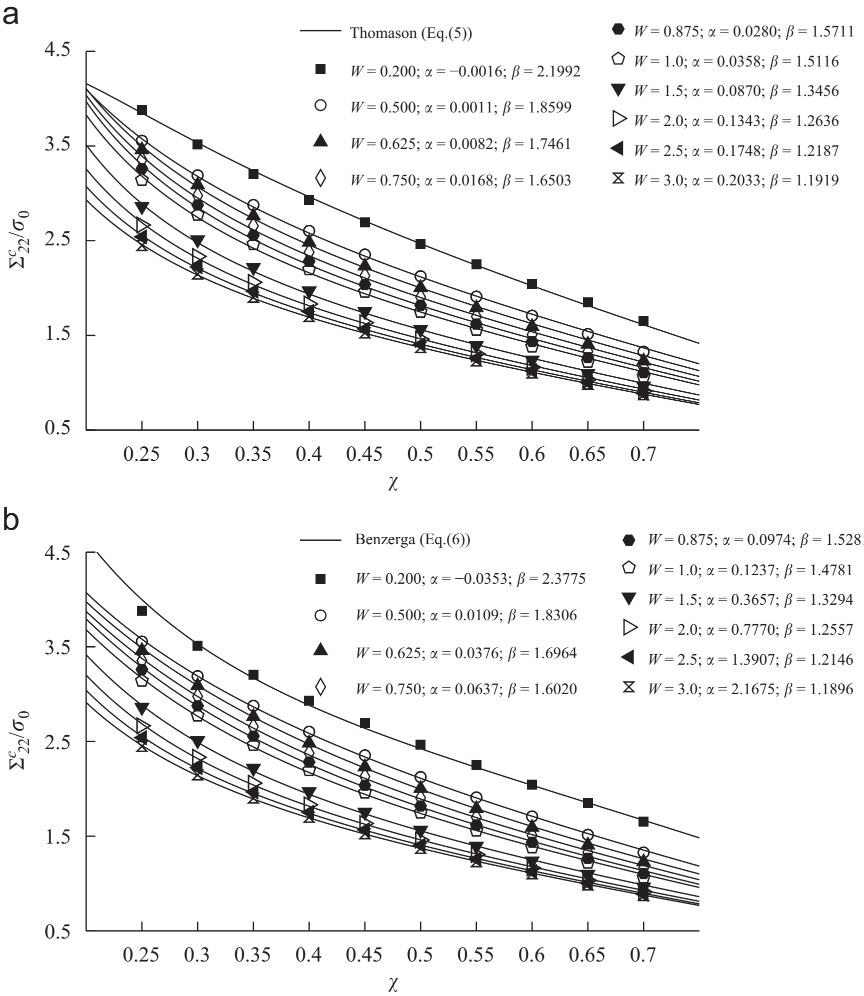

Fig. 6. Evolution of Σ_{22}^c/σ_0 as a function of χ, for different W values. Data points are the results of the FE calculations, while each solid line represents the best fit obtained by fine-tuning the α and β values for the corresponding W value, for the (a) original criterion of Thomason, Eq. (5), and (b) extension of Thomason's criterion by Benzerga, Eq. (6).

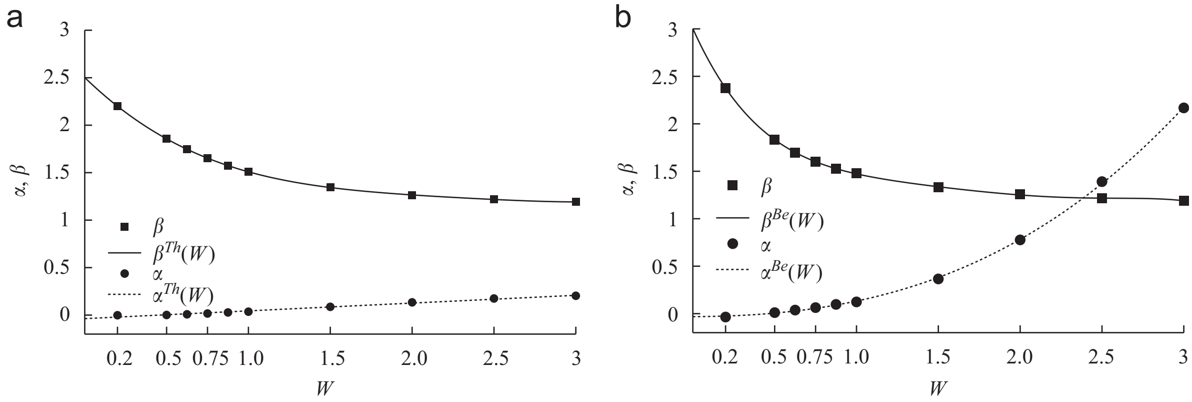

Fig. 7. Evolution of the parameters α and β as a function of W giving the best fits of the (a) original criterion of Thomason, Eq. (5), and (b) extension of Thomason's criterion by Benzerga, Eq. (6), to the FE data.

produce excellent agreement with the 3D FE unit cell calculations for void coalescence under tension. Note that the parameters α and β appearing in the original Thomason's criterion, Eq. (5), were also initially proposed by fitting numerical results obtained using assumed velocity fields.

Both $\beta(W)$ and $\alpha(W)$ can be expressed in terms of lesser degree polynomials at the cost of a reduction in accuracy; here, a high level of accuracy is deliberately provided to avoid contributions from the error associated with the coalescence criterion for pure tension to the generalized coalescence model developed in the next section.

4. A void coalescence criterion for general loadings

In the following, a void coalescence criterion is developed for general loading conditions. Unlike the criterion of Thomason – or its extension by Benzerga – for which the RVE is subjected to a predominant axial stress state with no shear component (i.e. $\Sigma_{22} > \Sigma_{11}$, $\Sigma_{22} > \Sigma_{33}$, $\Sigma_{21} = \Sigma_{23} = \Sigma_{13} = 0$), here, a general stress state is considered with non-zero shear components ($\Sigma_{22} > \Sigma_{11}$, $\Sigma_{22} > \Sigma_{33}$, $\Sigma_{21}(=\Sigma_{12}) \neq 0$, $\Sigma_{23}(=\Sigma_{32}) \neq 0$, see Fig. 8).

The new criterion developed in this study depends only on the stress components Σ_{22}, Σ_{21} and Σ_{23}. Indeed, when elasticity is negligible, the plastic behavior of the material is described by the theory of limit-analysis. A classical result of limit-analysis asserts that the property of normality, if assumed to be obeyed at the local scale, also holds at the global scale. Now consider the case [$\Sigma_{22} > \Sigma_{11}$, $\Sigma_{22} > \Sigma_{33}$, $\Sigma_{21} \neq 0$, $\Sigma_{23} \neq 0$, $\Sigma_{13} \neq 0$] and assume that coalescence is taking place. Since the strain rate components $D_{11} = D_{33} = D_{13} = 0$ (because the layers above and below the localization band remain rigid), and since the components D_{ij} are proportional to $\partial\phi/\partial\Sigma_{ij}$ (where ϕ is the macroscopic yield function), $\partial\phi/\partial\Sigma_{11} = \partial\phi/\partial\Sigma_{33} = \partial\phi/\partial\Sigma_{13} = 0$, that is ϕ depends only on Σ_{22}, Σ_{21}, and Σ_{23}. This is indeed why Σ_{22}^c is independent of stress triaxiality T, see Fig. 4(a).

As also stated by Leblond and Mottet (2008), considering the complexity of Thomason's analysis already in the problem with no shear, to perform the same analysis for a general stress state based on the detailed description of the microscopic velocity field around the void, if possible, would be a daunting task. Instead, we employ an RVE in the form of a "sandwich" made of three superposed planar layers, sound/porous/sound (see Fig. 8), and assume that during coalescence the sound

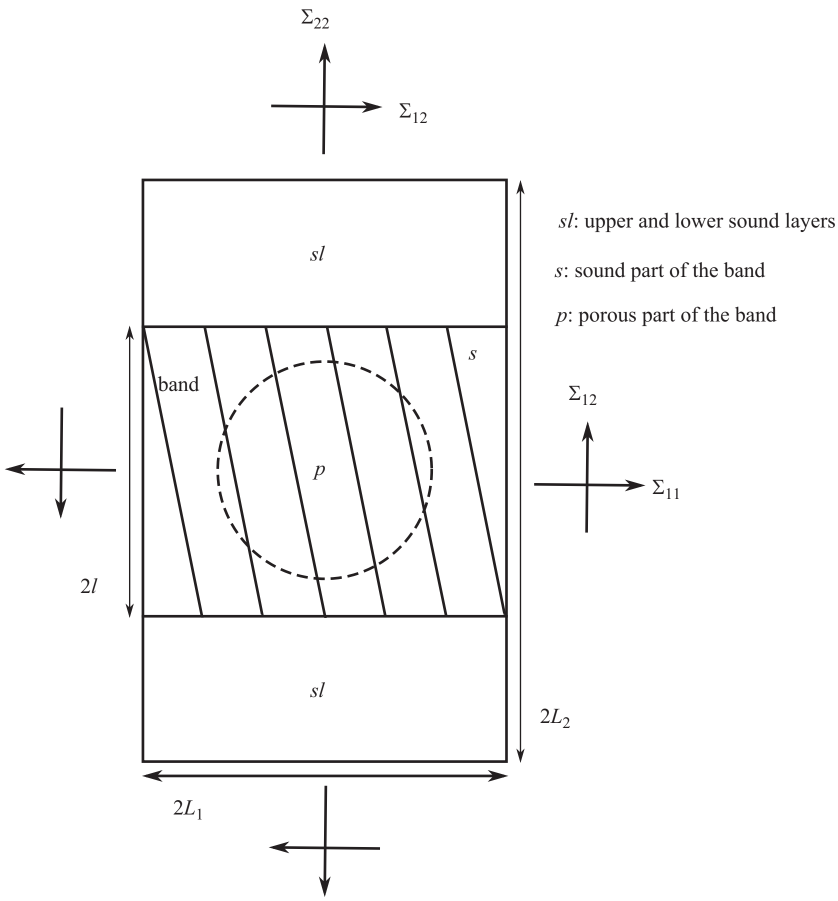

Fig. 8. The sandwich model.

layers become rigid while the velocity field in the central porous layer is given by

$$\mathbf{v}(\mathbf{r}) = D_{22}\mathbf{v}^{Th}(\mathbf{r}) + \mathbf{v}^{x_1}(\mathbf{r}) + \mathbf{v}^{x_3}(\mathbf{r}), \tag{11}$$

for which the strain rate tensor $\mathbf{d}(\mathbf{r}) = 1/2(\Delta\mathbf{v}(\mathbf{r}) + (\Delta\mathbf{v})^T(\mathbf{r}))$ reads

$$\mathbf{d}(\mathbf{r}) = D_{22}\mathbf{d}^{Th}(\mathbf{r}) + \mathbf{d}^{x_1}(\mathbf{r}) + \mathbf{d}^{x_3}(\mathbf{r}), \tag{12}$$

where $\mathbf{r}$ is the position vector, and the superscript (Th) indicates that the quantity to which it refers is exactly the same as in the original Thomason's (or Benzerga's) void coalescence criterion, developed for pure tension. Also, the velocities $\mathbf{v}^{x_i}(\mathbf{r})$ $(i = 1, 3$, no summation on $i)$ are defined as

$$\mathbf{v}^{x_i}(\mathbf{r}) = \begin{cases} \dfrac{2x_2}{c} D_{2i}\mathbf{e}_i & -l \le x_2 \le l, \\ \dfrac{-2l}{c} D_{2i}\mathbf{e}_i & x_2 < -l, \\ \dfrac{2l}{c} D_{2i}\mathbf{e}_i & x_2 > l, \end{cases} \tag{13}$$

where $c = l/L_2$, and $\mathbf{e}_i$ are the unit vectors codirectional with the x_i axes. The components of the strain rate tensor associated with the velocity fields $\mathbf{v}^{x_i}(\mathbf{r})$ read

$$d_{2i}^{x_i} = \begin{cases} \dfrac{1}{c} D_{2i} & -l \le x_2 \le l, \\ 0 & x_2 < -l \text{ and } x_2 > l. \end{cases} \tag{14}$$

An upper estimate of the plastic dissipation can be given as

$$\mathbf{\Pi}^+(\mathbf{d}) = \langle \sigma_0 d_{eq} \rangle_{RVE} = c\langle \sigma_0 d_{eq} \rangle_{band} = c\Big[(1-f_b)\langle \sigma_0 d_{eq} \rangle_s + f_b \langle \sigma_0 d_{eq} \rangle_p\Big], \tag{15}$$

where $\langle x \rangle_\Omega$ denotes the average of x over the domain Ω, d_{eq} is the equivalent strain rate, and f_b is the porosity in the band. Note that, for a central porous band in the form of a rectangular prism and a spheroidal void shape, as shown in Fig. 8, the ratio of f_b to the total porosity in the RVE, f, reads

$$\frac{f_b}{f} = \begin{cases} \dfrac{1}{c} = \dfrac{L_2}{l} & l \ge R_2, \\ \left(1 - \dfrac{l^2}{3R_2^2}\right)\dfrac{3}{2}\dfrac{L_2}{R_2} & l < R_2, \end{cases} \tag{16}$$

where R_2 is the radius of the void in the x_2 direction. Because the stress in the porous part of the band is zero, $\mathbf{\Pi}^+(\mathbf{d})$ reduces to

$$\mathbf{\Pi}^+(\mathbf{d}) = c(1-f_b)\sigma_0 \langle d_{eq} \rangle_s = c(1-f_b)\sigma_0 \left\langle \frac{1}{2}\Big(d_{eq}(x_1,x_2,x_3) + d_{eq}(x_1,-x_2,x_3)\Big)\right\rangle_s, \tag{17}$$

and since $\frac{1}{2}(a+b) \le \sqrt[2]{\frac{1}{2}(a^2+b^2)}$

$$\mathbf{\Pi}^+(\mathbf{d}) \le \mathbf{\Pi}^{++}(\mathbf{d}) = c(1-f_b)\sigma_0 \left\langle \sqrt[2]{\frac{1}{2}\Big(d_{eq}^2(x_1,x_2,x_3) + d_{eq}^2(x_1,-x_2,x_3)\Big)}\right\rangle_s. \tag{18}$$

The square of the equivalent strain rate d_{eq}^2 can be written as

$$\begin{aligned} d_{eq}^2 = \tfrac{2}{3}\,\mathbf{d}(\mathbf{r}) : \mathbf{d}(\mathbf{r}) = D_{22}^2(d_{eq}^{Th})^2 + \tfrac{2}{3}\Big[&2D_{22}\mathbf{d}^{Th}(\mathbf{r}) : \mathbf{d}^{x_1}(\mathbf{r}) + 2D_{22}\mathbf{d}^{Th}(\mathbf{r}) : \mathbf{d}^{x_3}(\mathbf{r}) \\ &+ \mathbf{d}^{x_1}(\mathbf{r}) : \mathbf{d}^{x_1}(\mathbf{r}) + \mathbf{d}^{x_3}(\mathbf{r}) : \mathbf{d}^{x_3}(\mathbf{r}) + 2\mathbf{d}^{x_1}(\mathbf{r}) : \mathbf{d}^{x_3}(\mathbf{r})\Big], \end{aligned} \tag{19}$$

and noting that $\mathbf{d}^{x_i}(\mathbf{r}) : \mathbf{d}^{x_j}(\mathbf{r}) = 0$ for $(i,j = 1, 3;\ i \ne j)$

$$\begin{aligned} \frac{1}{2}\Big(d_{eq}^2(x_1,x_2,x_3) + d_{eq}^2(x_1,-x_2,x_3)\Big) &= \frac{D_{22}^2}{2}\left[\left(d_{eq}^{Th}\right)^2(x_1,x_2,x_3) + \left(d_{eq}^{Th}\right)^2(x_1,-x_2,x_3)\right] \\ &+ \frac{4}{3}D_{22}\frac{D_{21}}{c}\Big(d_{21}^{Th}(x_1,x_2,x_3) + d_{21}^{Th}(x_1,-x_2,x_3)\Big) + \frac{4}{3}D_{22}\frac{D_{23}}{c}\Big(d_{23}^{Th}(x_1,x_2,x_3) + d_{23}^{Th}(x_1,-x_2,x_3)\Big) + \frac{4}{3}\frac{D_{21}^2 + D_{23}^2}{c^2}. \end{aligned} \tag{20}$$

As d_{eq}^{Th}, d_{21}^{Th}, and d_{23}^{Th} are, respectively, even, odd, and odd functions of x_2, Eq. (20) reduces to

$$\frac{1}{2}\Big(d_{eq}^2(x_1,x_2,x_3) + d_{eq}^2(x_1,-x_2,x_3)\Big) = D_{22}^2\left(d_{eq}^{Th}\right)^2 + \frac{4}{3}\frac{D_{21}^2 + D_{23}^2}{c^2}, \tag{21}$$

and Eq. (18) becomes

$$\mathbf{\Pi}^+(\mathbf{d}) \le \mathbf{\Pi}^{++}(\mathbf{d}) = c(1-f_b)\sigma_0 \left\langle \sqrt[2]{D_{22}^2\left(d_{eq}^{Th}\right)^2 + \frac{4}{3}\frac{D_{21}^2 + D_{23}^2}{c^2}}\right\rangle_s. \tag{22}$$

If we assume that

$$\left\langle \sqrt[2]{f^2+a} \right\rangle \approx \sqrt[2]{\langle f \rangle^2+a}, \tag{23}$$

where f is a positive function and a is a positive constant, the inequality (22) can be written as

$$\mathbf{\Pi}^+(\mathbf{d}) \leq \mathbf{\Pi}^{++}(\mathbf{d}) = c(1-f_b)\sigma_0 \sqrt[2]{D_{22}^2 \langle d_{eq}^{Th} \rangle_s^2 + \frac{4}{3}\frac{D_{21}^2+D_{23}^2}{c^2}}, \tag{24}$$

and the components of the stress tensor Σ_{ij} can be found as

$$\begin{aligned}
\Sigma_{22} &= \frac{\partial \mathbf{\Pi}^{++}(\mathbf{d})}{\partial D_{22}} = c^2(1-f_b)^2\sigma_0^2 \langle d_{eq}^{Th} \rangle_s^2 \frac{D_{22}}{\mathbf{\Pi}^{++}(\mathbf{d})}, \\
\Sigma_{21} &= \frac{1}{2}\frac{\partial \mathbf{\Pi}^{++}(\mathbf{d})}{\partial D_{21}} = \frac{2}{3}(1-f_b)^2\sigma_0^2 \frac{D_{21}}{\mathbf{\Pi}^{++}(\mathbf{d})}, \\
\Sigma_{23} &= \frac{1}{2}\frac{\partial \mathbf{\Pi}^{++}(\mathbf{d})}{\partial D_{23}} = \frac{2}{3}(1-f_b)^2\sigma_0^2 \frac{D_{23}}{\mathbf{\Pi}^{++}(\mathbf{d})}.
\end{aligned} \tag{25}$$

Now, it is straightforward to show that

$$\frac{\Sigma_{22}^2}{c^2(1-f_b)^2\sigma_0^2 \langle d_{eq}^{Th} \rangle_s^2} + \frac{3(\Sigma_{21}^2+\Sigma_{23}^2)}{(1-f_b)^2\sigma_0^2} = \frac{(\mathbf{\Pi}^{++}(\mathbf{d}))^2}{(\mathbf{\Pi}^{++}(\mathbf{d}))^2} = 1. \tag{26}$$

Repeating this derivation for $D_{21} = D_{23} = 0$, one can show that the maximum value of $|\Sigma_{22}^{Th}|$ provided by the limit-load analysis of Thomason is $\Sigma_{22}^{Th} = c(1-f_b)\sigma_0 \langle d_{eq}^{Th} \rangle_s$; therefore, Eq. (26) can be written as

$$\left(\frac{\Sigma_{22}}{\Sigma_{22}^{Th}}\right)^2 + \frac{3(\Sigma_{21}^2+\Sigma_{23}^2)}{(1-f_b)^2\sigma_0^2} = 1. \tag{27}$$

The equality in (23) is exact only if f is constant or if a is zero. Therefore, Eqs. (24) and (27) are approximations instead of rigorous upper bounds.

4.1. Comparison with the FE calculations

To validate the new coalescence criterion, FE calculations are performed with $E_{11}=E_{33}$ and $R_{sh} = E_{12}/E_{22} > 0$, where a macroscopic stress state $\Sigma_{22} > \Sigma_{11}$, $\Sigma_{22} > \Sigma_{33}$, $\Sigma_{12}(=\Sigma_{21}) \neq 0$ is imposed on the unit cell (for the technical details on the FE calculations, see Section 2). Two different relative void spacing values are evaluated ($\chi = 0.4$, 0.6) for each of the six different void aspect ratios ($W = 0.5k$, with $k = 1, \ldots, 6$). For each $W-\chi$ set, eighteen different R_{sh} values are used ($R_{sh} = 0.5k$, with $k = 0, \ldots, 10, 20, 30, 40, 80, 120, 160, 200$). Fig. 9 plots the axial stress Σ_{22} versus shear stress Σ_{12} for W=0.5 and $\chi = 0.4$. For each R_{sh} value, four sets of data are plotted, each corresponding to a different E_{11}/E_{22} ratio. Between the four sets of data, for the same R_{sh}, both Σ_{22} and Σ_{12} values are the smallest for the set with the largest E_{11}/E_{22} ratio ($= -2^{-2}$). With decreasing E_{11}/E_{22}, both Σ_{22} and Σ_{12} increase and converge to certain values, Σ_{22}^c and Σ_{12}^c, which represent, respectively, the normal and shear stress values required to initiate coalescence for the corresponding R_{sh}. Except for the data set with the largest E_{11}/E_{22}, all

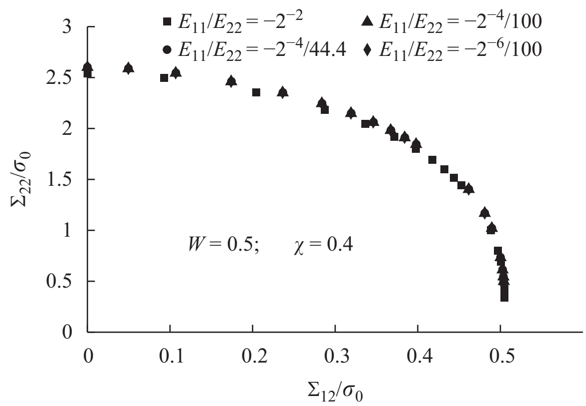

Fig. 9. Axial stress, Σ_{22}, versus shear stress, Σ_{12}, for $W = 0.5$, $\chi = 0.4$, obtained by the FE unit cell calculations. Eighteen different R_{sh} values are used ($R_{sh} = 0.5k$, with $k = 0, \ldots, 10, 20, 30, 40, 80, 120, 160, 200$), and for each R_{sh}, four sets of data are plotted, each corresponding to a different E_{11}/E_{22} ratio. Σ_{22} and Σ_{12} obtained for the smallest E_{11}/E_{22} ratio ($= -2^{-6}/100$) represent, respectively, Σ_{22}^c and Σ_{12}^c, i.e. the normal and shear stress values required to initiate coalescence for the corresponding R_{sh} value.

corresponding data points are nearly on top of each other, which ensures that Σ_{22} and Σ_{12} obtained for the smallest E_{11}/E_{22} ratio $(=-2^{-6}/100)$ represent the converged values.

For the stress state of the unit cell during void coalescence, Eq. (27) reads

$$\Sigma_{22}^{c}=\Sigma_{22}^{Th}\sqrt{1-\frac{3(\Sigma_{12}^{c})^{2}}{(1-f_{b})^{2}\sigma_{0}^{2}}}. \tag{28}$$

Σ_{22}^{Th} can be calculated using either of Eqs. (9) and (10) given in Section 3.4. The very accurate representations for the parameters α and β involved in Eqs. (9) and (10) ensures that validation of the new coalescence criterion with shear correction is not affected by other sources of error. Now, Eq. (28) can be validated using the results of the FE calculations; inserting Σ_{22}^{Th} and Σ_{12}^{c} (given by the FE results) in Eq. (28) should ideally provide the same value of Σ_{22}^{c} as obtained with the FE unit cell calculations. Note however that there is still one yet undetermined parameter in Eq. (28), f_b, i.e. the porosity in the band where the internal necking is observed, which is defined in Eq. (16). Comparison of Σ_{22}^{c} obtained using Eq. (28) with the results of the FE calculations showed that the best agreement between the two is attained for a band thickness of

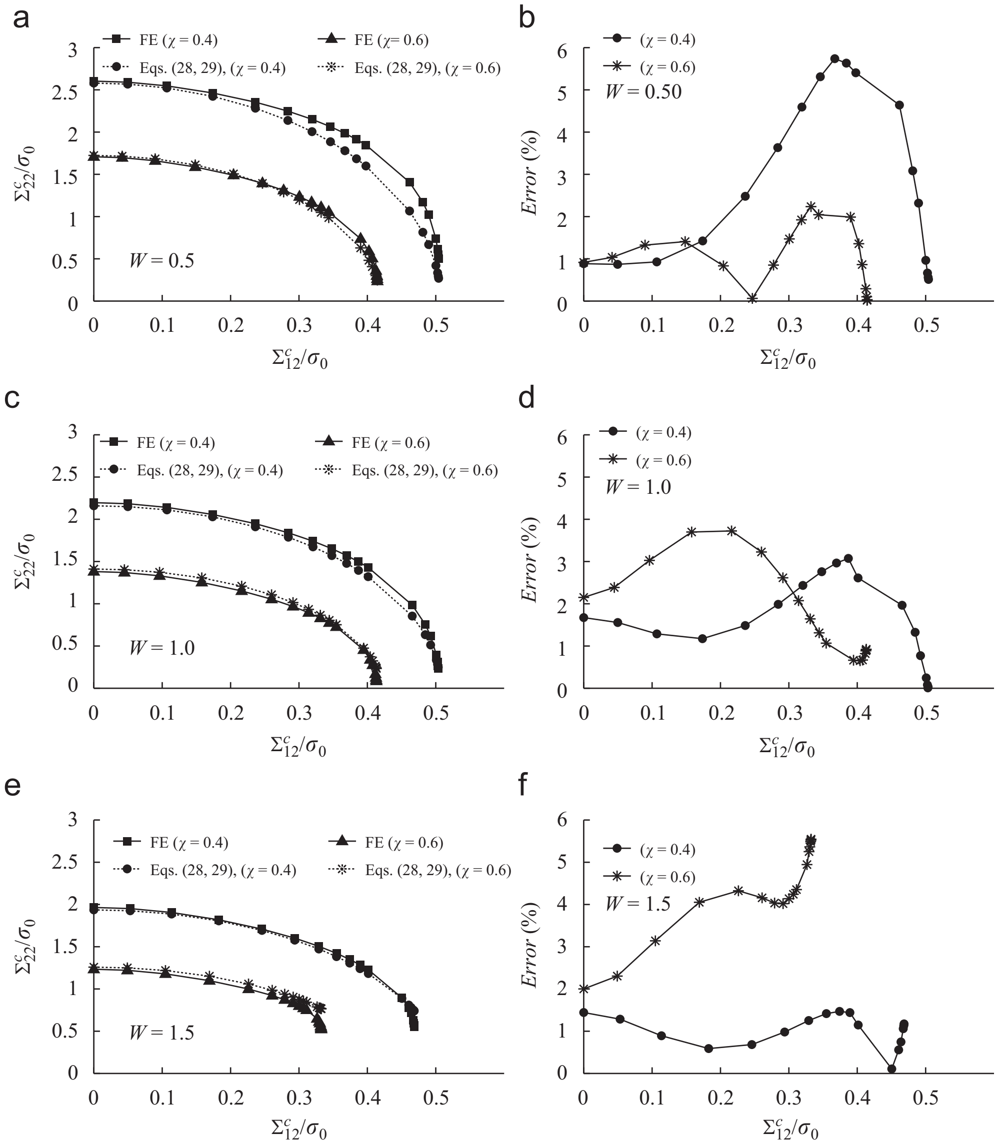

Fig. 10. (a, c, e, g, i, and k) The evolution of Σ_{22}^{c} as a function of Σ_{12}^{c} while comparing the values of Σ_{22}^{c} obtained by using Eqs. (28) and (29) with the results of the FE calculations, respectively, for six different void aspect ratios ($W=0.5k$, with $k=1,\ldots,6$), and for two χ values ($\chi=0.4,0.6$) at each W. (b, d, f, h, j, and l) The error – as defined in Eq. (30) – in the predictions of Eqs. (28) and (29). Note that for each $W-\chi$ set, 18 different $R_{sh}=E_{12}/E_{22}$ values are tested ($R_{sh}=0.5k$, with $k=0,\ldots,10,20,30,40,80,120,160,200$).

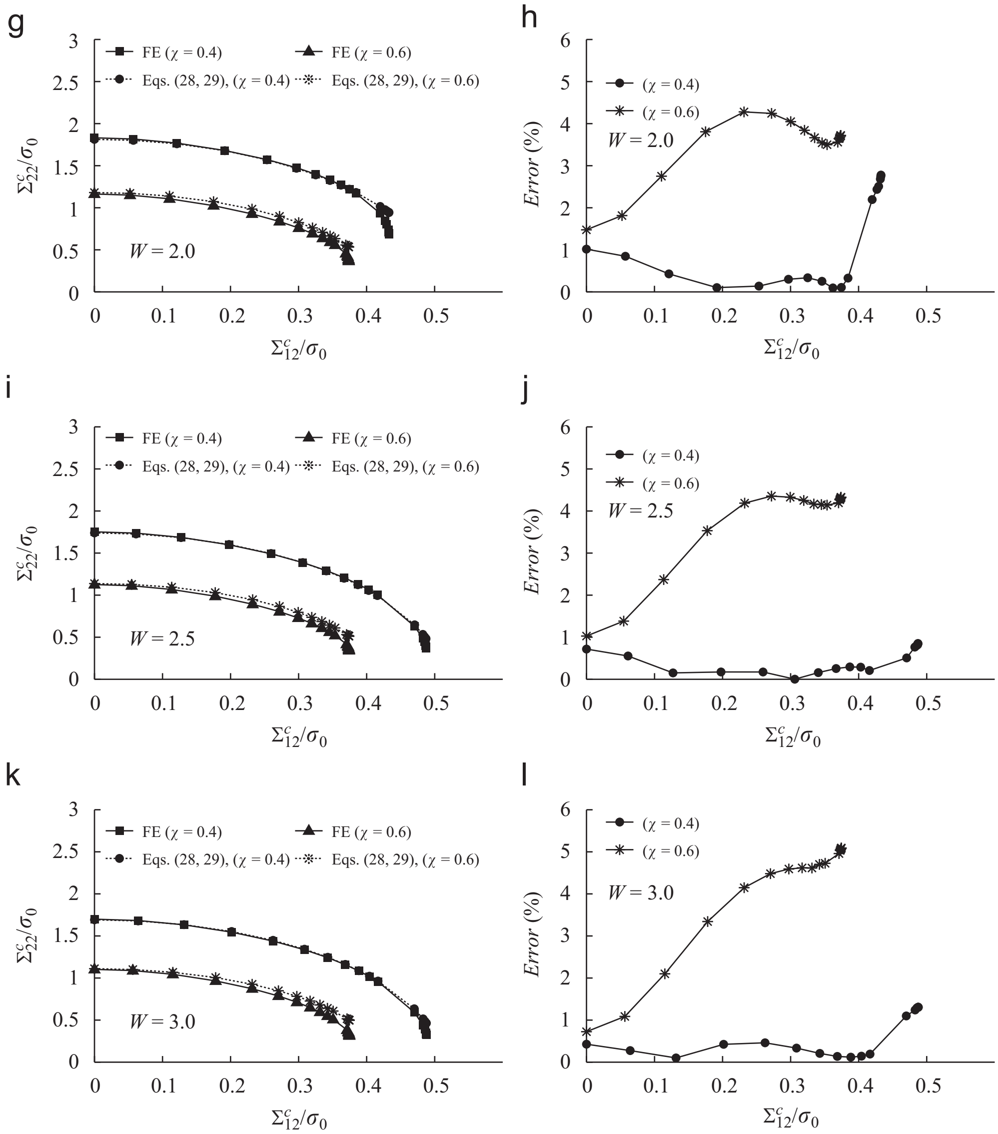

Fig. 10. (*continued*)

$2l=0.6R_2$, corresponding to an f_b value of

$$f_b=1.455\frac{L_2}{R_2}f=1.455\frac{L_2}{\chi WL_1}f. \tag{29}$$

The size and shape of the plastic deformation localization band is further discussed in Section 5.

Fig. 10(a), (c), (e), (g), (i), and (k) compare the values of Σ_{22}^c obtained using Eqs. (28) and (29) with the results of the FE calculations, respectively, for six different void aspect ratios ($W=0.5k$, with $k=1,\ldots,6$), and for two χ values ($\chi=0.4,0.6$) at each W. A separate convergence test – as shown in Fig. 9 – is performed for each $W-\chi$ set. Fig. 10(b), (d), (f), (h), (j), and (l) show the error in the predictions of Eqs. (28) and (29), which is defined as

$$\text{Error (\%)}=\left|\frac{QP}{QO}\right|\times 100, \tag{30}$$

where $O(0,0)$ is the origin of the $\Sigma_{12}^c-\Sigma_{22}^c$ plane, and $P((\Sigma_{12}^c)_{FE},(\Sigma_{22}^c)_{FE})$ and $Q((\Sigma_{12}^c)_{Eqs.(28,29)},(\Sigma_{22}^c)_{Eqs.(28,29)})$ are two data points at which a straight line originating from the point O intersects the $\Sigma_{12}^c-\Sigma_{22}^c$ curves obtained, respectively, through the FE calculations, and using Eqs. (28) and (29): $|QP|$ is the distance between the theoretical and the FE results, and $|QO|$ between the theoretical result and the origin. For each $W-\chi$ set, the error is evaluated on eighteen different lines, each passing from a different point Q obtained for a different R_{sh} value.

Similar tendencies are observed for all $W-\chi$ sets analyzed. With increasing R_{sh}, Σ_{22}^{c} decreases while Σ_{12}^{c} increases. For the same W, both Σ_{22}^{c} and Σ_{12}^{c} are lower for the larger χ value ($\chi=0.6$), and both stress values decrease with increasing W; the decrease in Σ_{22}^{c} with increasing W is more pronounced compared to that of Σ_{12}^{c}. For all $W-\chi$ sets, a very good agreement is observed between the FE results and the predictions of Eqs. (28) and (29): the error remains less than $\approx 6\%$ in the entire range of R_{sh} values. For $W\geq 1.5$, the predictions of Eqs. (28) and (29) are closer to the FE results for $\chi=0.4$ than for $\chi=0.6$; for $W<1.5$ there is no such tendency.

5. Discussion

In its original form, the model of Thomason does not produce accurate predictions for the axial stress value required to initiate coalescence, Σ_{22}^{c}, even for loadings that do not involve a shear component, and especially when the shape of the void is flat ($W<1$). Predictions of Benzerga's model better match the FE results, especially for small void aspect ratio (W) and small relative void spacing (χ) values, for which Thomason's model severely overestimates the FE data (see Fig. 5(d) and (c), respectively). To improve the predictive capability of both models, the parameters α and β incorporated are fine-tuned through comparison with the FE data and written as a function of W: $\beta(W)$ is a fifth order polynomial for both models, while $\alpha(W)$ is linear for Thomason's model and a third order polynomial for Benzerga's model (see Eqs. (7) and (8)). The improved Thomason's and Benzerga's criteria (Eqs. (9) and (10), respectively) are now equally accurate in the range of the FE calculations performed in this paper. As it inherently accounts better for penny-shaped/flat voids, Benzerga's criterion might be the best choice for very small W values outside the range of parameter calibration.

The new void coalescence model developed for general loading conditions is in very close agreement with the FE results, see Section 4. In order to build the new model, we employed an RVE similar to that of Leblond and Mottet (2008) and Perrin (1992), i.e. a "sandwich" made of three superposed planar layers, sound/porous/sound. The present model, however, is much closer in spirit to that of Thomason than to that of Leblond and Mottet (2008) since it is clearly based on limit-analysis and on a completely specified trial velocity field. In Leblond and Mottet (2008), no explicit trial velocity field was provided, and an extra assumption that "the limit-load of the RVE may be evaluated by schematizing the RVE as a sandwich, with Gurson's model approximately describing the behavior of the central porous layer" was introduced.

The new coalescence model does not incorporate any fitting parameters other than $\beta(W)$ and $\alpha(W)$; both are associated with the original criterion of Thomason (and its extension by Benzerga) which is used to calculate Σ_{22}^{Th} (Note again that, the parameters α and β appearing in the original Thomason's criterion, Eq. (5), were also initially proposed by fitting numerical results obtained using assumed velocity fields). As also pointed out by Benzerga and Leblond (2010), knowledge of the exact shape and size of the localized plastic deformation band is not needed for coalescence under pure tension. For coalescence under general loading, however, the porosity in the localized plastic deformation band, f_b, and therefore, the size of the band directly enters the coalescence criterion. Fig. 11 shows the equivalent plastic strain distribution at the onset of void coalescence for W=0.5 and (a) $\chi=0.4$, $R_{sh}=0$, (b) $\chi=0.6$, $R_{sh}=0$, (c) $\chi=0.4$, $R_{sh}=5$, (d) $\chi=0.6$, $R_{sh}=5$, (e) $\chi=0.4$, $R_{sh}=20$, (f) $\chi=0.6$, $R_{sh}=20$, where $R_{sh}=E_{12}/E_{22}$ is the ratio of the shear strain to the axial strain. In all these cases, plastic strain is confined in the intervoid ligament – concentrating mainly in the close neighborhood of the void – while the remaining parts of the unit cell unload elasticity. However, the thickness of the localized deformation band ($2l$) as well as the magnitude of the strain concentration (SC) depend on both the relative void spacing χ and the strain ratio R_{sh}: l and SC are lower for the larger χ value, and for both χ values, l decreases while SC increases with increasing R_{sh}. Fig. 11 clearly shows that the localization band has an irregular shape, and f_b is a state variable which should ideally depend on the void shape/size and on the stress state of the unit cell. Here, however, for convenience, we assumed that the localization band is a rectangular prism whose thickness depends solely on the void radius aligned in the direction of the predominant axial stress (R_2). In this case, the maximum f_b for a spheroidal void is attained when the thickness of the band $2l$ goes to 0, with $f_b^{max}=1.5(L_2/R_2)f$ (where L_2 is the half length of the RVE and f is the overall porosity in the RVE, see Eq. (16). As shown in Fig. 10, the best agreement between the new coalescence criterion and the FE results is obtained for a band thickness of $2l=0.6R_2$, for which the porosity in the band reads $f_b=1.455(L_2/R_2)f$. Note that the optimal value of f_b is very close to f_b^{max}; this is satisfactory. Indeed, in limit-analysis, the best value of the limit-load that can be provided, i.e. the minimum value of the theoretical limit-load, correspond to f_b^{max}; this, however, is not rigorously true here because of the approximations introduced in the analysis performed in Section 4.

The strain levels in Fig. 11 might seem rather large to allow performing the calculations while switching off the non-linear geometry option (NLGEOM=No; for technical details see ABAQUS (2008b)). As explained in Section 2 (and in Appendix), in order to guarantee that the limit load is reached, i.e. the order of magnitude of the elastic strains in the unit cell is much smaller than the order of magnitude of the plastic strains, we applied rather large displacements for all void configurations ($W-\chi$ sets). Fig. 12(a) and (b) show the equivalent plastic strain distribution at the onset of void coalescence for $W=0.5$, $\chi=0.4$, $R_{sh}=0$, as in Fig. 11(a), but, compared to Fig. 11(a), the absolute values of the displacements applied at the boundaries of the unit cell are 10 times smaller in (a), and 20 times smaller in (b). It is clear that the thickness and the shape of the localized deformation band, as well as the relative magnitude of the strain concentration in the band are virtually the same in all three figures. Fig. 12(c) shows the stress–strain diagram for the unit cell with $W=0.5, \chi=0.4, R_{sh}=0$. We clearly see that the rather small initial elastic deformation regime is followed by a large perfectly plastic regime. From left to right, the cross signs indicate the axial stress value required to initiate coalescence, Σ_{22}^{c}, for the calculations performed in Figs. 12(a) and (b) and 11(a), respectively. The value of Σ_{22}^{c} is only 0.11% (resp. 0.5%) less for Fig. 12(a) (resp. Fig. 12(b)) compared to Fig. 11(a). Note also that each cross sign

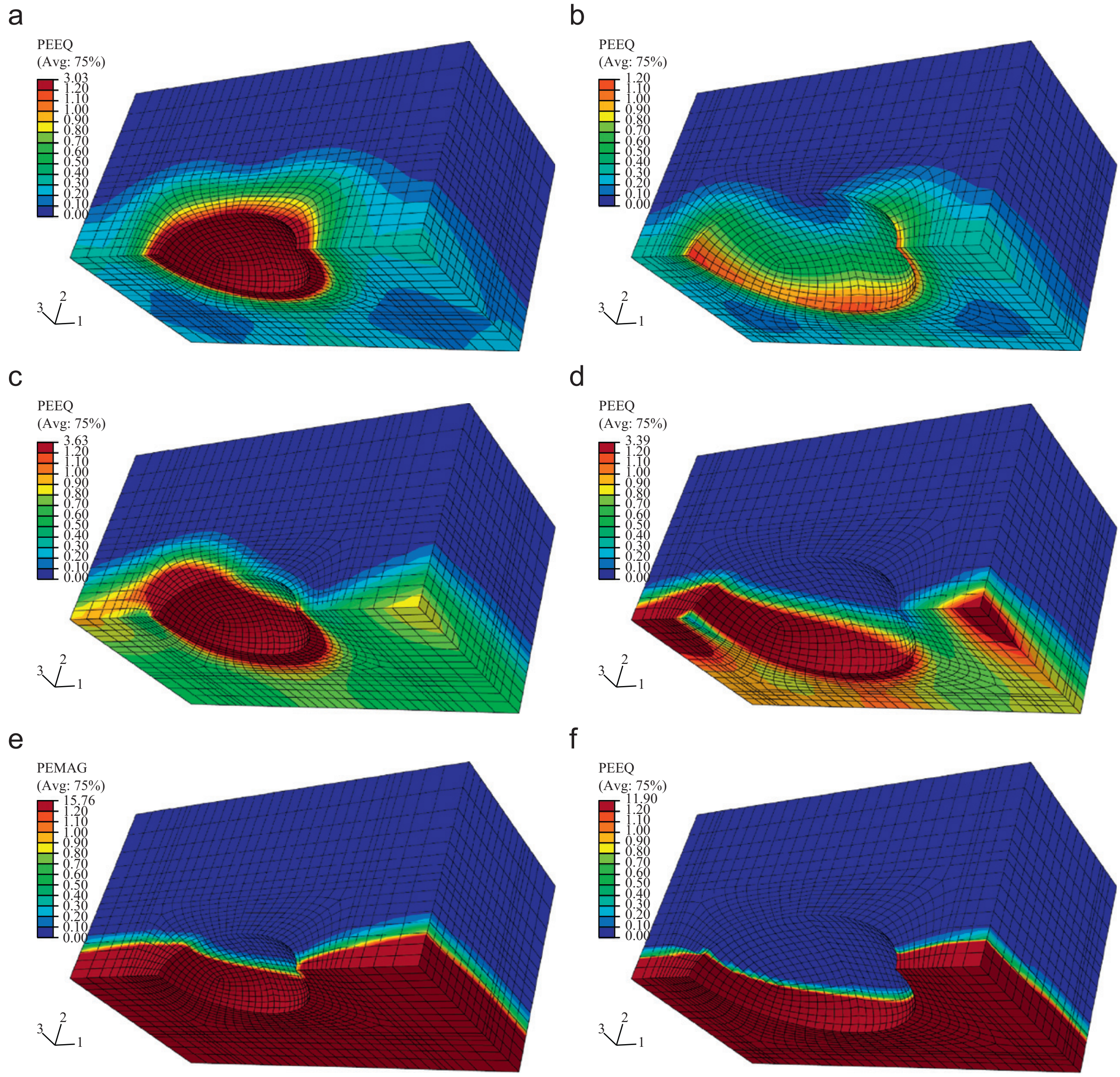

Fig. 11. Distribution of equivalent plastic strain at the onset of void coalescence for $W=0.5$ and (a) $\chi=0.4$, $R_{sh}=0$, (b) $\chi=0.6$, $R_{sh}=0$, (c) $\chi=0.4$, $R_{sh}=5$, (d) $\chi=0.6$, $R_{sh}=5$, (e) $\chi=0.4$, $R_{sh}=20$, (f) $\chi=0.6$, $R_{sh}=20$, where $R_{sh}=E_{12}/E_{22}$ is the ratio of the shear strain to the axial strain.

is located at the applied macroscopic strain value for the corresponding calculation, i.e. $E_{22}=0.05, =0.005, =0.0025$ for, respectively, Figs. 11(a) and 12(a) and (b). To summarize, applying smaller (respectively, larger) displacements at the boundaries leads to smaller (respectively, larger) local displacements by the same factor, but the stress field does not change. This justifies again switching NLGEOM off for the calculations performed in this paper.

To emphasize again, here we focus on the coalescence of voids while suppressing the void growth phase to maintain the prescribed void shape at coalescence. When, however, a coalescence model itself is incorporated into an FE code to investigate ductile fracture of a sample or of a structure, geometry changes should be taken into account in the damage model, with an update of the criterion at every time step (for details see e.g. Tvergaard, 2008, 2009, and recently Dahl et al., 2012). One may note that the development of the original Thomason model followed exactly the same steps: first, the model was developed with the aid of limit analysis, where the limit load was defined without accounting for geometry changes; then the model was connected to a damage model accounting for such changes.

Accurate modeling of coalescence under general loading conditions is vital when dealing with problems such as "cup–cone" fracture of smooth axisymmetric specimens, investigated by several authors; e.g. Besson et al. (2001), Devaux et al. (1992), and Tvergaard and Needleman (1984). In this problem, the final deviation of the crack plane from its original

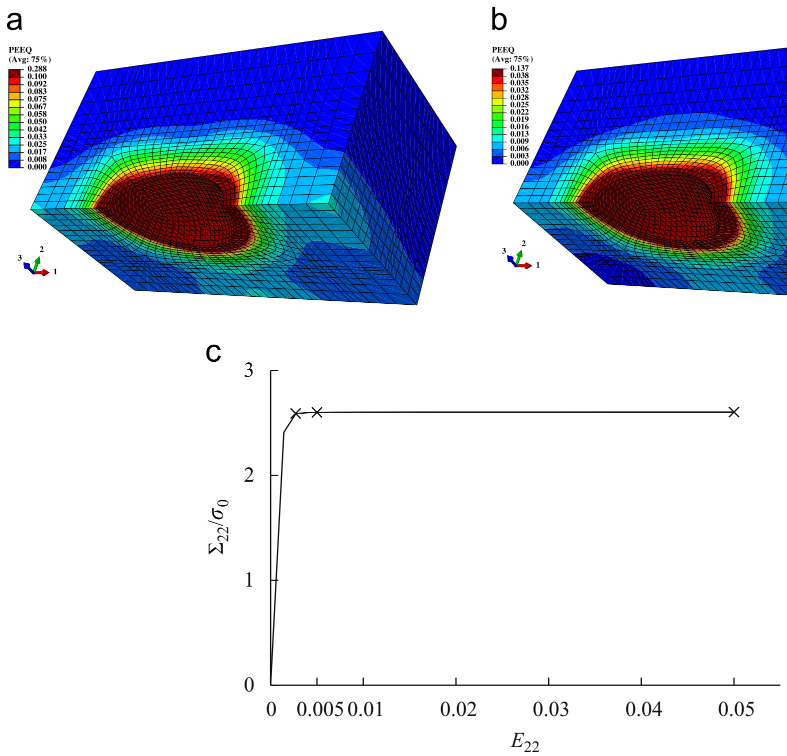

Fig. 12. (a and b) Distribution of equivalent plastic strain at the onset of void coalescence for $W=0.5$, $\chi=0.4$, $R_{sh}=0$, as in Fig. 11(a). Compared to Fig. 11(a), however, the absolute values of the displacements applied at the boundaries of the unit cell are 10 times smaller in (a), and 20 times smaller in (b). (c) Stress–strain diagram for the unit cell with $W=0.5$, $\chi=0.4$, $R_{sh}=0$. From left to right, the cross signs indicate the axial stress value required to initiate coalescence, Σ_{22}^c, for the calculations performed in (b), (a), and Fig. 11(a), respectively. Note that the value of Σ_{22}^c is only 0.11% (resp. 0.5%) less for (a) (resp. (b)) compared to Fig. 11(a), and that each cross sign is located at the applied macroscopic strain value for the corresponding calculation, i.e. $E_{22}=0.05, =0.005, =0.0025$ for, respectively, Figs. 11(a), 12(a), and 12(b).

orientation is at 45°, implying that the local stress state at the crack tip includes a large shear component. Other examples involve some forming or cutting operations including large shear deformations. In the course of ductile crack growth in mixed mode (mode I and mode II) conditions, shear stress components are suspected to play an important role (see e.g. Xue et al., 2010 and references therein); for a large K_{II}/K_I ratio, that is if high shear stresses are imposed, the crack propagates along its original direction, which, most probably, coincides with a shear band that develops in this direction. Following the same lines as, for example, in the work of Pardoen et al. (2010) dealing with inclined soft bands undergoing large shear deformations, such interesting problems can be investigated through large scale FE models by implementing the coalescence model developed here into FE codes.

6. Conclusions

The outcome of this study is twofold; the original void coalescence model of Thomason has been: (i) improved by fine-tuning its coefficients and (ii) extended for general loading conditions. A very extensive set of FE calculations has been performed on 3D voided unit cells and used as the benchmark against the theoretical predictions in both parts of the study. The main conclusions of this study are:

- The new coalescence criterion developed for general loading conditions involving shear, Eq. (27), produces very accurate predictions: the error remains less than $\approx 6\%$ for the entire range of FE calculations performed for various void configurations and various loading conditions.
- The improved criterion of Thomason and of Benzerga for pure tension (Eqs. (9) and (10), respectively) are equally and highly accurate over the large range of FE calculations performed in this paper. Compared to Thomason's original criterion, the extension of Benzerga has the advantage that it works much better for penny-shaped/flat voids even in its original form and is thus a good choice for very small void aspect ratio values, falling outside the range examined in this paper.

- The criterion of Brown and Embury (Eq. (2)) is purely geometric and does not take the stress state into account. In contradiction with the FE calculations, it states that for a certain void aspect ratio W there is a minimum relative intervoid distance χ below which coalescence cannot initiate, irrespective of the stress state. However, this criterion can still provide qualitative predictions for coalescence under low stress triaxiality.

Appendix A. Plastic limit-load analysis with the finite element method

Plastic limit-load analysis of a structure Ω corresponds to a problem of small strain plasticity with no elasticity, which can be expressed through the following equations:

$$\begin{cases} \text{div}\ \boldsymbol{\sigma} = 0 \\ \mathbf{d} = \frac{1}{2}\{\nabla_{\mathbf{X}}\mathbf{v} + [\nabla_{\mathbf{X}}\mathbf{v}]^T\} \\ f(\boldsymbol{\sigma}) \le 0 \\ \mathbf{d} = \dot{\eta}\frac{\partial f}{\partial \boldsymbol{\sigma}}(\boldsymbol{\sigma}) \\ \dot{\eta}\begin{cases} = 0 & \text{if } f(\boldsymbol{\sigma}) < 0 \\ \ge 0 & \text{if } f(\boldsymbol{\sigma}) = 0 \end{cases} \end{cases} \quad \text{in } \Omega,$$
$$+\text{Boundaryconditions.} \tag{A.1}$$

In these equations, $\mathbf{X}$ is the position vector in the initial configuration, $\mathbf{v}$ the velocity, $\mathbf{d}$ the strain rate, $\boldsymbol{\sigma}$ the stress tensor, $f(\boldsymbol{\sigma})$ the von Mises yield function, and η the plastic multiplier.

Assume that, to solve this problem, the finite element method is used with an implicit (backward Euler) algorithm for the projection of the elastic stress predictor onto the yield locus, in a single large step with no geometry update. Let $\boldsymbol{\sigma}_0 = 0$, $\boldsymbol{\sigma}_1$, $\boldsymbol{\varepsilon}_0 = 0$, $\boldsymbol{\varepsilon}_1$, $\mathbf{u}_0 = 0$, $\mathbf{u}_1$ denote, respectively, the initial (subscript "0") and the final (subscript "1") stresses, strains, and displacements for the structure Ω. Provided that the load increment is large enough to ensure that the order of magnitude of the elastic strains in the structure is much smaller than the order of magnitude of the plastic strains, the equations of the time-discretized problem read:

$$\begin{cases} \text{div}\ \boldsymbol{\sigma}_1 = 0 \\ \boldsymbol{\varepsilon}_1 = \frac{1}{2}\{\nabla_{\mathbf{X}}(\mathbf{u}_1) + [\nabla_{\mathbf{X}}(\mathbf{u}_1)]^T\} \\ f(\boldsymbol{\sigma}_1) \le 0 \\ \boldsymbol{\varepsilon}_1 - \boldsymbol{\varepsilon}_0 = \boldsymbol{\varepsilon}_1 \simeq \Delta\eta\frac{\partial f}{\partial \boldsymbol{\sigma}}(\boldsymbol{\sigma}_1) \\ \Delta\eta\begin{cases} = 0 & \text{if } f(\boldsymbol{\sigma}_1) < 0 \\ \ge 0 & \text{if } f(\boldsymbol{\sigma}_1) = 0 \end{cases} \end{cases} \quad \text{in } \Omega,$$
$$+\text{Boundary conditions.} \tag{A.2}$$

The equation systems in A.1 and A.2 are equivalent; $\boldsymbol{\sigma}$, $\mathbf{v}$, and $\mathbf{d}$ in A.1 correspond, respectively, to $\boldsymbol{\sigma}_1$, $\mathbf{u}_1$, and $\boldsymbol{\varepsilon}_1$ in A.2. The key point here is that, in the discretized flow rule, $\partial f/\partial \boldsymbol{\sigma}$ is taken at the point $\boldsymbol{\sigma}_1$ instead of $\boldsymbol{\sigma}_0 = 0$.

The equivalence of A.1 and A.2 leads to the conclusion that a problem of plastic limit-load analysis can be solved by the standard elastoplastic finite element method, if the load is applied in a single step sufficiently large to ensure that the elastic strains in the structure are much smaller than the plastic strains. Note again that the equation system A.2 is derived with respect to the initial (undeformed) geometry; while performing the FE calculations with ABAQUS, this is taken into account by employing the "NLGEOM=No" option. From the results of the FE calculations, one may obtain the plastic limit-load (from the stresses), the velocity field (which is proportional to the displacement field), as well as the strain rate field (which is proportional to the strain field).

References

ABAQUS, 2008a. Analysis User's Manual, Section 23.1.1, Solid (Coninuum) Elements (Subsection: Choosing an Appropriate Element), The Abaqus Documentation Collection, Version 6.8. Providence. Dassault Systèmes, Rhode Island.

ABAQUS, 2008b. Analysis User's Manual, Section 6.1.2, General and Linear Perturbation Procedures (Subsection: Sources of Nonlinearity), The Abaqus Documentation Collection, Version 6.8. Providence. Dassault Systèmes, Rhode Island.

Argon, A., Im, J., Safoglu, R., 1975. Cavity formation from inclusions in ductile fracture. Metall. Mater. Trans. A 6, 825–837.

Bandstra, J.P., Koss, D.A., 2001. Modeling the ductile fracture process of void coalescence by void-sheet formation. Mater. Sci. Eng. A 319–321, 490–495.

Becker, R., 1987. The effect of porosity distribution on ductile failure. J. Mech. Phys. Solids 35, 577–599.

Benzerga, A.A., 2000. Rupture ductile des tôles anisotropes. Ph.D. Thesis. Ecole Nationale Supérieure des Mines de Paris.

Benzerga, A.A., 2002. Micromechanics of coalescence in ductile fracture. J. Mech. Phys. Solids 50, 1331–1362.

Benzerga, A.A., Besson, J., Pineau, A., 2004. Anisotropic ductile fracture. Part I: experiments. Acta Mater. 52, 4623–4638.

Benzerga, A.A., Leblond, J.-B., 2010. Ductile fracture by void growth to coalescence. Adv. Appl. Mech. 44, 169–305.

Besson, J., Steglich, D., Brocks, W., 2001. Modelling of crack growth in round bars and plane strain specimens. Int. J. Solids Struct. 38, 8259–8284.

Brown, L.M., Embury, J.D., 1973. The initiation and growth of voids at second phase particles. In: Proceedings of the Third International Conference on Strength of Metals and Alloys. ICSMA 3, Institute of Metals, Cambridge, UK, pp. 164–169.
Cox, T., Low, J., 1974. An investigation of the plastic fracture of aisi 4340 and 18 nickel-200 grade maraging steels. Metall. Mater. Trans. B 5, 1457–1470.
Dahl, J., Nielsen, K.L., Tvergaard, V., 2012. Effect of contact conditions on void coalescence at low stress triaxiality shearing. J. Appl. Mech. 79 doi:10.1115/1.4005565.
Devaux, J., Leblond, J.-B., Mottet, G., Perrin, G., 1992. Some new applications of damage models for ductile metals. In: Application of Local Fracture/Damage Models to Engineering Problems, Proceedings of the 1992 ASME Summer Mechanics Meeting. American Society of Mechanical Engineers, Tempe (USA).
Fabrègue, D., Pardoen, T., 2008. A constitutive model for elastoplastic solids containing primary and secondary voids. J. Mech. Phys. Solids 56, 719–741.
Fabrègue, D., Pardoen, T., 2009. Corrigendum to "A constitutive model for elastoplastic solids containing primary and secondary voids". J. Mech. Phys. Solids 57, 869–870.
Gologanu, M., Leblond, J.-B., Devaux, J., 2001a. Theoretical models for void coalescence in porous ductile solids. II. Coalescence in columns. Int. J. Solids Struct. 38, 5595–5604.
Gologanu, M., Leblond, J.-B., Perrin, G., Devaux, J., 2001b. Theoretical models for void coalescence in porous ductile solids. I. Coalescence in layers. Int. J. Solids Struct. 38, 5581–5594.
Koplik, J., Needleman, A., 1988. Void growth and coalescence in porous plastic solids. Int. J. Solids Struct. 24, 835–853.
Kuna, M., Sun, D.Z., 1996. Three-dimensional cell model analyses of void growth in ductile materials. Int. J. Fract. 81, 235–258.
Lassance, D., Scheyvaerts, F., Pardoen, T., 2006. Growth and coalescence of penny-shaped voids in metallic alloys. Eng. Fract. Mech. 73, 1009–1034.
Leblond, J.-B., Mottet, G., 2008. A theoretical approach of strain localization within thin planar bands in porous ductile materials. C.R. Mec. 336, 176–189.
Lecarme, L., Tekoğlu, C., Pardoen, T., 2011. Void growth and coalescence in ductile solids with stage III and stage IV strain hardening. Int. J. Plast. 27, 1203–1223.
Marini, B., Mudry, F., Pineau, A., 1985. Experimental study of cavity growth in ductile rupture. Eng. Fract. Mech. 6, 989–996.
McClintock, F.A., 1968. A criterion for ductile fracture by the growth of holes. J. Appl. Mech. 35, 363–371.
McClintock, F.A., 1971. Plasticity aspects of fracture. In: Liebowitz, H. (Ed.), Fracture—An Advanced Treatise, vol. 3. Academic Press, pp. 47–225.
Needleman, A., 1972. Void growth in an elastic-plastic medium. J. Appl. Mech. 39, 964–970.
Nielsen, K.L., Tvergaard, V., 2011. Failure by void coalescence in metallic materials containing primary and secondary voids subject to intense shearing. Int. J. Solids Struc. 48, 1255–1267.
Pardoen, T., 2006. Numerical simulation of low stress triaxiality ductile fracture. Comput. Struct. 84, 1641–1650.
Pardoen, T., Bréchet, Y., 2004. Influence of microstructure-driven strain localization on the ductile fracture of metallic alloys. Philos. Mag. 84, 269–297.
Pardoen, T., Doghri, I., Delannay, F., 1998. Experimental and numerical comparison of void growth models and void coalescence criteria for the prediction of ductile fracture in copper bars. Acta Mater. 46, 541–552.
Pardoen, T., Hutchinson, J.W., 2000. An extended model for void growth and coalescence. J. Mech. Phys. Solids 48, 2467–2512.
Pardoen, T., Hutchinson, J.W., 2003. Micromechanics-based model for trends in toughness of ductile metals. Acta Mater. 51, 133–148.
Pardoen, T., Scheyvaerts, F., Simar, A., Tekoğlu, C., Onck, P.R., 2010. Multiscale modeling of ductile failure in metallic alloys. C.R. Phys. 11, 326–345.
Perrin, G., 1992. Contribution 'a l' étude th éorique et num érique de la rupture ductile des m étaux. Ph.D. Thesis. Ecole Polytechnique, Palaiseau, France.
Pineau, A., Pardoen, T., 2007. Failure Mechanisms of Metals, vol. 2. Elsevier (Chapter 6).
Richelsen, A., Tvergaard, V., 1994. Dilatant plasticity or upper bound estimates for porous ductile solids. Acta Metall. Mater. 42, 2561–2577.
Scheyvaerts, F., Onck, P.R., Tekoğlu, C., Pardoen, T., 2011. The growth and coalescence of ellipsoidal voids in plane strain under combined shear and tension. J. Mech. Phys. Solids 59, 373–397.
Scheyvaerts, F., Pardoen, T., Onck, P.R., 2010. A new model for void coalescence by internal necking. Int. J. Damage Mech. 19, 95–126.
Simar, A., Nielsen, K.L., de Meester, B., Tvergaard, V., Pardoen, T., 2010. Micro-mechanical modelling of ductile failure in 6005a aluminium using a physics based strain hardening law including stage IV. Eng. Fract. Mech. 77, 2491–2503.
Tekoğlu, C., Pardoen, T., 2010. A micromechanics based damage model for composite materials. Int. J. Plast. 26, 549–569.
Thomason, P.F., 1985. A three-dimensional model for ductile fracture by the growth and coalescence of microvoids. Acta Metall. 33, 1087–1095.
Thomason, P.F., 1990. Ductile Fracture of Metals, 1st ed. Pergamon Press, Oxford, England.
Tvergaard, V., 1990. Material failure by void growth to coalescence. Adv. Appl. Mech. 27, 83–151.
Tvergaard, 2008. Shear deformation of voids with contact modeled by internal pressure. Int. J. Mech. Sci. 50, 1459–1465.
Tvergaard, 2009. Behaviour of voids in a shear field. Int. J. Fract. 158, 41–49.
Tvergaard, V., Needleman, A., 1984. Analysis of cup–cone fracture in a round tensile bar. Acta Metall. 32, 157–169.
Tvergaard, V., Nielsen, K.L., 2010. Relations between a micro-mechanical model and a damage model for ductile failure in shear. J. Mech. Phys. Solids 58, 1243–1252.
Xue, Z., Pontin, M., Zok, F., Hutchinson, J., 2010. Calibration procedures for a computational model of ductile fracture. Eng. Fract. Mech. 77, 492–509.
Yerra, S.K., Tekoğlu, C., Scheyvaerts, F., Delannay, L., Houtte, P.V., Pardoen, T., 2010. Void growth and coalescence in single crystals. Int. J. Solids Struct. 47, 1016–1029.